Lithuanian Journal of Physics, Vol. **45**, No. 6, pp. 423–436 (2005)

MICROWAVE RADIATION AND X-RAY-INDUCED PHENOMENA IN SEMICONDUCTORS

S. Ašmontas [a,b], A. Laurinavičius [a], J. Paukštė [b], and A. Šilėnas [a]

[a] *Semiconductor Physics Institute, A. Goštauto 11, LT-01108 Vilnius, Lithuania*
E-mail: asmontas@uj.pfi.lt
[b] *Panevėžys Institute, Kaunas University of Technology, Klaipėdos 1, LT-35209 Panevėžys, Lithuania*

Received 21 December 2005

We review experimental results on interaction of microwave and X-rays with various semiconductors that have been obtained at the Semiconductor Physics Institute starting from the pioneering works of J. Požela up to his latest achievements. Special attention is paid to the microwave technique allowing one to estimate the hot electron diffusion coefficient in semiconductors and the bigradient effect, the phenomenon which has been recognized as a discovery in 1977. The application aspects of the above research are furthered in two different approaches: in microwave range, this is done via non-destructive characterization of material homogeneity either by excitation of the helicon waves or by a local excitation of millimetre waves in the tested sample, while in X-ray range this is exposed in the application of inhomogeneous and graded-gap semiconductors to convert the X-rays into optical range thus enabling their detection by conventional CCD cameras.

Keywords: microwaves, helicons, hot carriers, semiconductor X-ray detectors

PACS: 61.82.Fk, 72.20.-i, 07.05.Pj, 78.70.-g, 29.40Wk

1. Introduction

Investigation of the interaction of electromagnetic radiation with semiconductors is in a particular focus of many scientists as it allows one not only to obtain information on the crystalline structure of these materials, but, also to employ their features in designing and fabricating new devices. In 1960, J. Požela suggested to use the microwave radiation to study the properties of semiconductors in strong electric fields [1]. Absorption of the microwaves by free carriers increases their mean energy, and, as a result, the electron temperature becomes higher than the lattice one. Such non-equilibrium carriers – so-called 'hot electrons' – exhibit new features in transport phenomena since their kinetic coefficients – diffusion coefficient and mobility – change under the influence of the electric field.

The application of various microwave technique to measure the drift velocity of charge carriers in strong electric fields enabled one to avoid carrier injection from contacts and to separate in a galvanic way the current circuit from that of the heating microwave fields. Therefore the usage of such an approach was successfully implemented in measuring the anisotropy of electrical conductivity in germanium and silicon [2], led to the discovery of the effect of absolute negative resistance for the dc current when a semiconductor is placed into alternating electric fields [3, 4], and allowed to measure the thermoelectromotive force of hot carriers, which was first done for Ge and Si [5]. The physical reason of the thermoelectromotive force of hot carriers in inhomogeneous structures is the change in carrier mobility and diffusion coefficient under the influence of microwave radiation [6]. Later, the technique was developed by different authors and was applied to estimate the diffusion coefficient and carrier relaxation times ([6] and the literature cited therein).

Magnetic field strongly changes the character of interaction of electromagnetic radiation of free carriers in semiconductors. For instance, in strong magnetic fields, the propagation of circularly polarized helicon waves along its direction is possible [7]. Investigation of reflection and transmission features of these waves can be a way to determine the electric parameters of the material [7–9]. This idea can serve as a basis in constructing relevant devices for material characterization [10, 11].

If the energy of an electromagnetic quantum is increased so that it exceeds the bandgap of a semiconductor, a number of new effects can be observed depending on the structure of that semiconductor. If it is in-

ISSN 1648-8504

homogeneously doped, the generation of electron–hole pairs, for example, by X-ray illumination, induces an electromotive force proportional to the intensity of the incident light [12]; if the semiconductor is non-uniform in composition, like in the graded-gap compounds, the ionizing illumination induces a photoluminescence in optical range that can be detected via conventional optical means [13].

The present paper reviews the results in experimental research on microwave and X-ray interaction with various semiconductors obtained at the Semiconductor Physics Institute starting from pioneering works of J. Požela up to his latest achievements.

The paper is organized as follows. Firstly, we describe one of the microwave techniques which allows one to determine the carrier diffusion coefficient in strong microwave electric fields and we consider in more detail the experimental conditions when non-conventional carrier transport manifests itself via the electron gas cooling effect; its possible applications will be discussed as well. Secondly, we will briefly introduce the physics behind the bigradient effect, the phenomenon which has been recognized as a discovery in 1977. The third chapter is on non-destructive material homogeneity characterization by millimetre waves giving special emphasis on the helicon waves. Finally, we focus our attention to the results devoted to the application of inhomogeneous and graded-gap semiconductors for converting X-rays into optical range and enabling hence to detect the ionizing illumination using conventional CCD cameras.

2. Features of non-equilibrium carrier transport in semiconductors

Application of microwave radiation allows one to simplify significantly the measurements of kinetic parameters of the semiconductors in strong electric fields. It can be easily understood from Fig. 1, where the measurement scheme to study the effect of microwave field is depicted schematically. The sample under the test was placed in the centre of a rectangular waveguide perpendicular to its wider walls. The samples were insulated from the waveguide by dielectric material; one can see that the heating circuit (microwave fields) is separated in a galvanic way from the measurement one. During the experiment, the change of the dc current induced by the alteration of carrier mobility and diffusion coefficient is measured. The typical I–V curves in germanium obtained using this approach at 10 GHz frequency range are given in Fig. 2. One can see that the

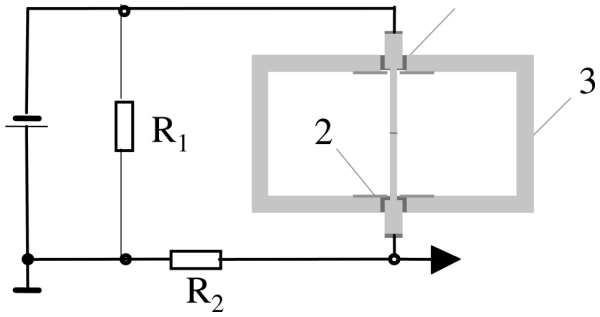

Fig. 1. Scheme of measurements of samples in microwave electric fields. *1* labels dielectric material for insulation, *2* is sample under test, *3* depicts rectangular waveguide.

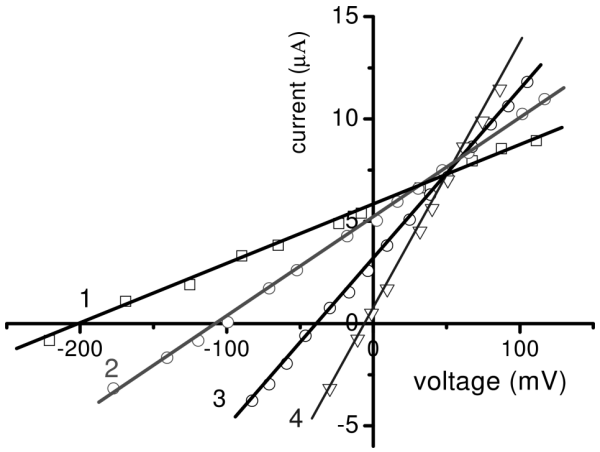

Fig. 2. I–V characteristics of n–n^+ germanium sample in heating microwave electric fields at room temperature. Smooth n–n^+ junction of 2 mm width was introduced during lithium diffusion process. Specific resistances in n- and n^+- parts of the junction are 38 Ω·cm and 7.3 Ω·cm, respectively. Numbers denote the strengths of the microwave electric fields, kV/cm: *1* is for 5.1, *2* for 3.15, *3* for 1.6, *4* for 0.

strong microwave electric field causes the asymmetry in the I–V characteristics. In inhomogeneous semiconductors containing $n-n^+$ junction, the asymmetry U_T that appears as a result of the microwave radiation-induced thermoelectromotive force of hot carriers is [14]:

$$U_T = V_{K0}\left(\frac{\overline{D}}{D_0}\frac{\mu_0}{\overline{\mu}_\mathrm{d}} - 1\right), \qquad (1)$$

where V_{K0} is the height of the potential barrier of the $n-n^+$ junction, $\overline{\mu}_\mathrm{d}$ and $\overline{D}$ are electron differential mobility and diffusion coefficient averaged over the microwave period, μ_0 and D_0 are the electron mobility and diffusion coefficients in a low electric field, respectively. If the ratio of mobilities changes negligibly with the electric field, U_T is then proportional to the change of the diffusion coefficient. The relation (1) is valid in the case of smooth $n-n^+$ junction and at high frequencies when the displacement currents are much greater

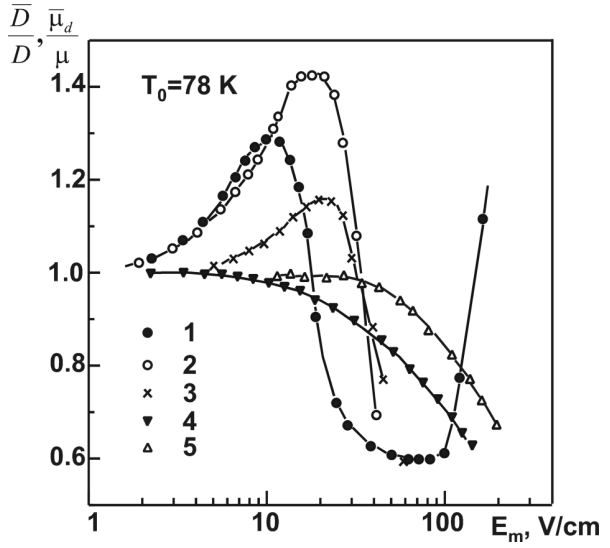

Fig. 3. Longitudinal (*1* and *3*, $\overline{D}_{\rm L}$) and transverse (*2*, $\overline{D}_{\rm T}$) hot electron diffusion coefficients and electron mobility $\mu_{\rm d}$ (*4* and *5*) as functions of the microwave electric field in highly compensated InSb: *1*, *2*, and *4* for 10 GHz, *3* and *5* for 35 GHz.

than the ohmic ones. Under these conditions therefore the carrier diffusion coefficient can be estimated in a semiconductor in strong electric fields. The technique was first demonstrated by estimating the electric field dependences of the electron diffusion coefficient in Ge [14].

In what follows we will restrict ourselves to a specific case of the diffusion processes when electrons behave non-conventionally in the heating electric fields, i. e. instead of the increase of diffusion with the electric field, the diffusion decreases and, even more, it might be lower than the value D_0 in the low electric field. The effect was discovered in highly compensated InSb, the inherent feature of which is the presence of random potential in the conduction band.

The dependences of hot electron diffusion coefficient (both longitudinal and transverse) on the microwave electric field are shown in Fig. 3. The samples of dumbbell-shape (in order to avoid contact effects) were prepared from the crystal of n-InSb grown by the Czochralski method. The concentration of doping impurities Cr (deep donor) and Mn or Zn (shallow acceptors) introduced during the growth was in the range of $2{\cdot}10^{15}$ cm^{-3}. Electron concentration and mobility at liquid nitrogen temperature were $n = (10^{10} - 10^{14})$ cm^{-3} and $\mu \approx 2.5 \cdot 10^5$ cm^2/(V·s), respectively. Since the carrier mobility changes negligibly in the studied electric fields, the observed strong decrease in diffusion coefficient with the electric field is caused by the decrease of mean electron energy[1] – it corresponds to the range where D is smaller than D_0 [15]. For the transverse diffusion coefficient this occurs in stronger electric fields as compared to the longitudinal case. In contrast, diffusion of warm electrons is isotropic due to the relaxation of the drift velocity and average energy of electrons in the microwave electric fields [15].

Similar dependence of D on the microwave electric field is obtained at the heating electric fields of 37 GHz (Fig. 3), however, its change in low fields is smaller and the range where$\overline{D} < D_0$ is shifted to stronger electric fields. We attributed this to the relaxation of the electron drift velocity and the influence of random potential of the conduction band [16].

Thus, as the diffusion coefficient reflects the change of the electron mean energy, one can consider the change of the mean electron energy with the electric field. The range where the diffusion coefficient is lower than D_0 deserves the particular attention. There the mean electron energy becomes smaller than the equilibrium one in the electric fields. Thus, we observe the effect of electron cooling by the heating electric field. The physical model can be described following the theoretical considerations by Gribnikov and Kochelap [17]: an electron, accelerated by the electric field, reaches the energy of optical phonon and emits an optical phonon; as a result, the electron losses all its energy and finds itself at the bottom of the conduction band. The electron is localized here, since its mobility is low due to the scattering on the complexes of ionized impurities. For that reason the mean electron energy becomes smaller than the equilibrium value. The increase of carrier concentration leads to the more intense electron–electron scattering which stimulates the delocalization of electrons from the bottom of the conduction band; consequently, the effect is destroyed [18].

The model of the electron gas cooling was evidenced experimentally by a transverse-to-current-flow magnetic field [19]. Since the emission of optical phonon is necessary for electron gas cooling, one can expect the absence of the effect in strong magnetic fields. The experiments confirmed the assumption: it was determined that the electron gas cooling vanishes in the magnetic field with induction $B > 0.05$ T ($\mu B > 1$), i. e. the suppression of optical phonon emission decreases the number of electrons that reach the bottom of the conduction band.

Therefore, for existence of the electron gas cooling effect the strict conditions must be met: firstly, the

[1] We have assumed that the Einstein relation is valid in this case

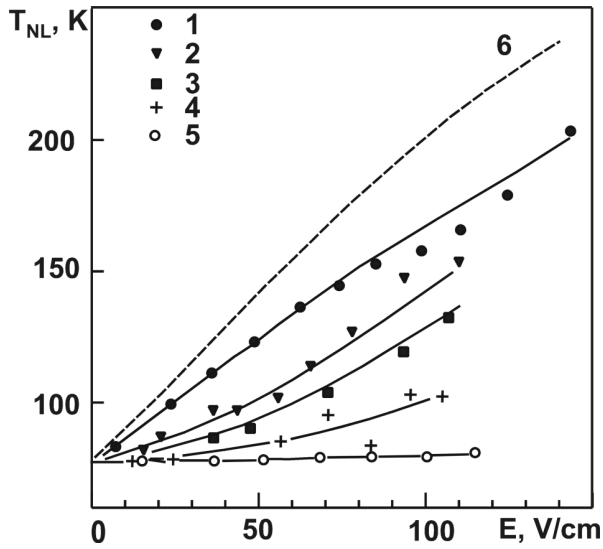

Fig. 4. Dependence of longitudinal noise temperature on the electric field at $T = 80$ K in the samples with different electron concentration, cm^{-3}: *1* for $4{\cdot}10^{12}$, *2* for $2{\cdot}10^{12}$, *3* for $1.5{\cdot}10^{12}$, *4* for $3{\cdot}10^{11}$, *5* for $8{\cdot}10^{10}$; *6* for $1.4{\cdot}10^{14}$ (broken curve – from [20]).

dominant mechanism of electron energy loss should be a spontaneous emission of optical phonons, secondly, electron should lose its momentum due to ionized impurity scattering, and, finally, the electron concentration must be low to avoid electron–electron interaction.

To reveal the application aspects of the electron gas cooling effect, the noise temperature was measured. As the mean electron energy in electric fields can be lower than the equilibrium value, the reduction in noise temperature is expected. The data on both longitudinal and transverse noise temperatures[2] revealed that with the decrease of electron concentration the noise temperature decreases, too, and in high resistivity samples (when the electron concentration becomes below $10^{11}\mathrm{cm}^{-3}$) the noise temperature in electric fields up to 100 V/cm does not depend on the electric field and is close to the lattice one (Fig. 4). One must note that such kind of noise temperature dependence is only observed in the samples where the inversion of U_T sign is observed. Moreover, the features of noise temperature in high resistivity samples in magnetic fields are similar to those of thermoelectromotive force at the same experimental conditions [21]. Hence it was inferred that the peculiarities observed in noise temperature were related to the electron gas cooling effect. Finally, it is worth noting that the decrease in noise temperature is of particular importance for practical purposes – it could

[2] The longitudinal and transverse noise temperatures were measured by applying pulses of dc electric field over the samples placed in the rectangular waveguide at 10 GHz frequency, as described in [20]

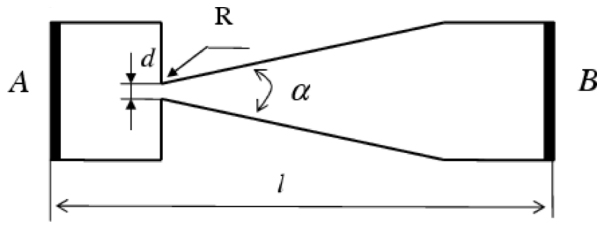

Fig. 5. Asymmetrically shaped n-Ge sample. Letters *A* and *B* denote ohmic contact areas. The area of the square part is $1.8 \cdot 10^{-5}\mathrm{cm}^2$, $\alpha \approx 24°$, $l = 2.4$ cm, the specific resistance is 10 Ω·cm.

be one of the options to increase the sensitivity of microwave detectors.

3. The bigradient effect in homogeneous semiconductors

As a rule, in many cases, the carrier heating in semiconductors is inhomogeneous due to the non-uniform electric fields. It is very important thus to understand the peculiarities of the non-equilibrium carriers under these conditions. One of the ways to realize the non-uniform carrier heating is to shape asymmetrically a homogeneous semiconductor. Such a sample is depicted in Fig. 5. As one can see further, the I–V characteristic of such a sample becomes asymmetric in strong electric fields. It is seen from Fig. 6 that two parts in I–V curves can be distinguished: the **low-voltage part** (up to 100 V), where the Ohm's law is fulfilled and the current flowing through the sample does not depend on the polarity of the applied voltage, and the **high-voltage part** (above 100 V) where the I–V curve deviates from the Ohm's law and becomes asymmetric, i. e. under the application of the same bias of different polarities, the current in the forward direction is higher than that in the reverse one. It is evident that a **uniform** Ge, if asymmetrically-necked shaped, in strong electric fields behaves like a conventional diode.

This phenomenon can be explained with the help of Fig. 7, where a schematic view of the sample is given and the distributions of the electric field and of average electron energy are depicted. We analyze the physical processes in a **uniform** asymmetrically-shaped n-type semiconductor sample under the application of external voltage of different polarity. It is evident that in the region $x_1 - x_2$ the electric field is non-uniform in comparison to that in $x_2 - x_3$ where the gradient of the electric field is much lower. At forward bias (denoted in part (a) as case *1*), the average electron energy $\varepsilon_1(x)$ at a certain distance x is smaller than that of a steady state in a uniform electric field, $\varepsilon(E)$. As a result, in the

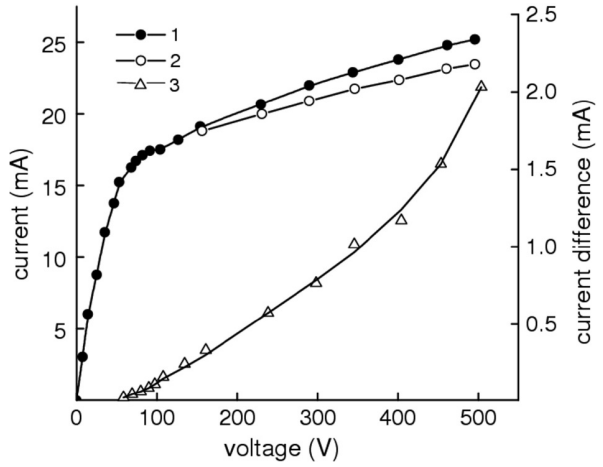

Fig. 6. I–V characteristics of the sample: *1* for forward bias, *2* for reverse bias, *3* for the difference of currents under the change of voltage polarity.

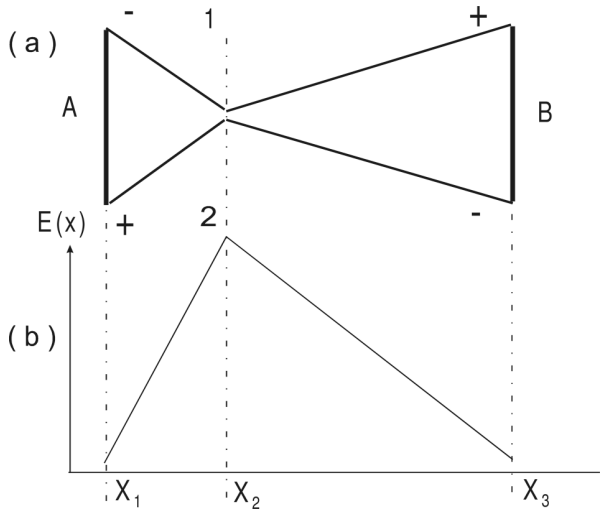

Fig. 7. (a) Schematic view of device shape, (b) distribution of the electric field, and (c) average electron energy along the sample. Letters *A* and *B* denote the contacts while numbers *1* and *2* label the polarity of the applied voltage (taken from [22]).

region $x_1 \leq x \leq x_2 + L_\varepsilon$ (L_ε is the product of electron drift velocity and energy relaxation time) the inequality $\varepsilon_1(x) < \varepsilon(E)$ is fulfilled. Usually, the mobility decreases with the increase of average electron energy, therefore, the situation $\mu_1(x) > \mu(E)$ is realized (here $\mu_1(x)$ and $\mu(E)$ designate the electron mobility as a function of coordinate and of a uniform electric field, respectively.)

At reverse bias, i. e. when the electrons move from the contact B to contact A (labelled as case *2* in part (a)), the average electron energy $\varepsilon_2(x)$ in the region $x_1 - x_2$ is larger than $\varepsilon(E)$. Thus, in the necked part of the sample $x_1 \leq x \leq x_2 + L_\varepsilon$, the electron mobility for the forward current is larger than that for the reverse one, i. e. $\mu_1(x) > \mu_2(x)$.

These findings not only illustrate the fact that the electron mobility in strongly non-uniform electric fields depends both on the electric field and its gradient, but also demonstrate that the current I_2 is larger than I_1 at the same value of applied voltage.

Thus, the effect, when such a shape induces non-uniform carrier heating in uniform semiconductor, is called **bigradient effect** (due to the **two** gradients of the electric field). Consequently, such asymmetrically-necked structures display asymmetry in their I–V characteristics. If such a sample is placed in a high-frequency field, the voltage signal – so-called bigradient electromotive force – will be induced over the ends of the structure.

One should note, however, that this simple description of the effect is only valid for relatively small electric fields. In higher fields, the described nonlocal relation of mobility to the electric field looses its importance compared to the role of space charge accumulation in the vicinity of the neck of the structure. As a result, the effect changes its sign: the current under the reverse bias becomes larger than under the forward one.

The bigradient effect – a phenomenon of arising of electromotive force and the asymmetry of electrical conductivity in uniform isotropic semiconductors – was recognized as a new phenomenon in semiconductor physics, and it was registered as a discovery [24] in the former Soviet Union.

Finally, it is worth mentioning that the idea of the bigradient effect was successfully used in designing the broad band THz sensors where a two-dimensional electron gas was implemented as an active ingredient in the device [25].

4. Nondestructive material homogeneity characterization by millimetre waves

4.1. Helicon wave beam in semiconductors

The circularly polarized electromagnetic wave propagating in the conductive medium along the external magnetic field is known as the helicon wave. These waves can be successfully used for contactless measurement of the semiconductor electrical parameters such as free charge carrier concentration and mobility [7, 26]. It is mainly determined by the dependence of helicon wave dispersion and attenuation on these parameters. On the other hand, the helicon wave features such as short wavelength in the material (Fig. 8) and its propagation along the external magnetic field direction (Fig. 9) give a possibility to focus these waves into

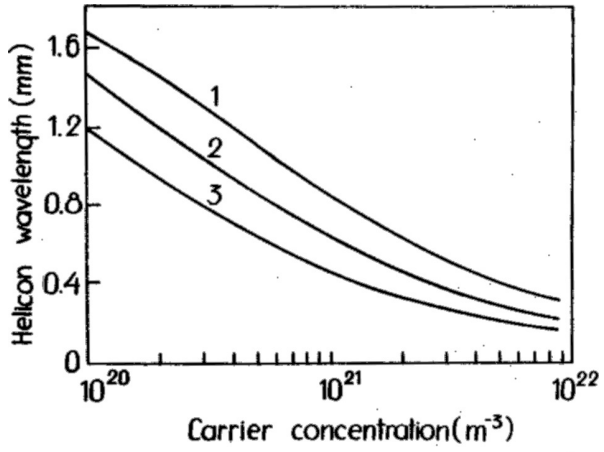

Fig. 8. Helicon wavelength dependence on free charge carrier concentration. Magnetic induction values are: *1* – $B = 1.0$ T, *2* – $B = 0.5$ T, *3* – $B = 0.25$ T. The wave frequency is 35 GHz.

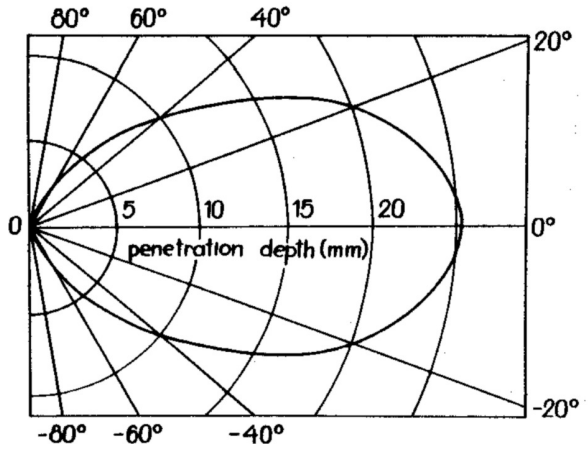

Fig. 9. The calculated angular dependence of helicon wave penetration depth. Semiconductor parameters are: $n = 1.6 \cdot 10^{20}$ m^{-3}, $\mu = 54$ m^2/(V·s). Wave frequency is 30.7 GHz. Magnetic induction is 0.6 T.

a narrow beam and to probe the semiconductor in its different points. The free charge carrier concentration and mobility measurement in different points of volume allows one to obtain the information about the crystal electrical homogeneity, and thus about its quality. The idea to use helicon waves for local measurements of free charge carrier concentration and its distribution in the crystal volume was suggested for the first time in the paper [27]. Later on, this idea was developed for the local measurement of both free charge carrier concentration and mobility [28]. The first helicon device for the characterization of electrical homogeneity of the semiconductor material was created about twenty years ago [29]. The helicon device is in principle the Rayleigh millimetre wave interferometer, the schematic diagram of which is shown in the left bottom corner of Fig. 10. The interferometer consists

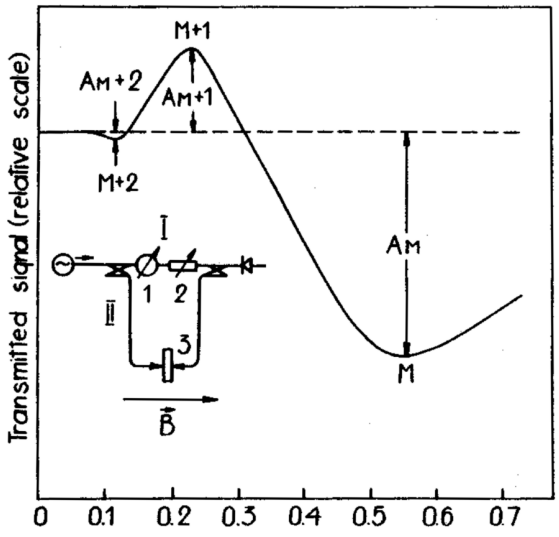

Fig. 10. The schematic diagram of helicon tester and a typical Rayleigh interferogram.

of the reference signal arm *I* and the sample arm *II*. The phase shifter *1* in the arm *I* is used for changing the phase of the reference signal, and the attenuator *2* serves to determine the interferometer sensitivity. The semiconductor plate *3* is placed in the sample arm between the special dielectric waveguide probes that provide the local excitation and reception of the helicon wave. The plate can be moved by the scanning mechanism in regard to the exciting and receiving probes in the x–y plane. The increase of the external magnetic field causes the changes in the amplitude and phase of the signal that is transmitted trough the plate and interferes with the reference signal. As a result the typical interferogram shown in Fig. 11 is obtained in the given point of the plate. By scanning the plate with the helicon beam in different points the information about the electrical homogeneity of the plate can be obtained. Thus, the helicon testing technique is very much like the ultrasonic one. The difference is only in the fact that the helicon testing can give the information on electrical homogeneity in a mechanically homogeneous crystal.

Such information is included in the period and the envelope of the interferograms measured in different points of the plate. This is clearly demonstrated by Fig. 11, where two Rayleigh interferograms measured at two different points of the $Hg_{0.8}Cd_{0.2}Te$ semiconductor plate are shown. The measurements were carried out at frequency of 37 GHz and temperature of 77 °K. The observed differences in the interferogram period and amplitude evidence an electrical inhomogeneity of the plate. The quantitative evaluation of electrical inhomogeneity can be obtained by

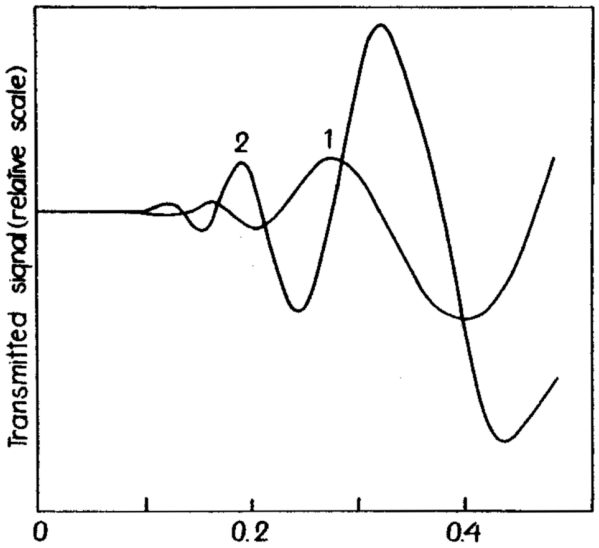

Fig. 11. Rayleigh interferograms measured at two different points of the electrically inhomogeneous semiconductor plate. The electron concentration and mobility values calculated from curves *1* and *2* correspond to $n = 3.6 \cdot 10^{21}$ m^{-3}, $\mu = 24.5$ m^2/(V·s) and $n = 5.3 \cdot 10^{21}$ m^{-3}, $\mu = 34.0$ m^2/(V·s), respectively.

the calculation of the free charge carrier concentration and mobility in every measured point according to the equations [30]

$$n = \frac{\varepsilon_0 \pi^2 c^2 I^2}{e\omega d^2} \cdot \frac{1}{\left(B_{M+1}^{-1/2} - B_M^{-1/2}\right)}, \qquad (2)$$

$$\mu = \frac{\pi I \left(B_{M+1}^{-1} + B_{M+1}^{-1/2} \cdot B_M^{-1/2} + B_M^{-1}\right)}{2 \ln \left[\frac{A_M}{A_{M+1}} \cdot \left(\frac{B_{M+1}}{B_M}\right)^{1/2}\right]}, \qquad (3)$$

where B_M and B_{M+1} are the magnetic induction values at which the interference extrema of the Mth and (M+1)th order are observed, A_M and A_{M+1} are the corresponding amplitudes of the extrema (see Fig. 10), d denotes the semiconductor plate thickness, ω is the wave angular frequency, c designates the light velocity, e is the electron charge, ε_0 labels the permittivity of free space, number I is an integer. It is seen from expressions that the concentration measurement accuracy is mainly determined by the precision of the measurement of the magnetic induction value at which the interference extrema are observed, while the mobility measurement accuracy depends in addition on the precision of the amplitude measurement of these extrema. The estimation of the relative error of the concentration and mobility measurement are also presented in the paper [30].

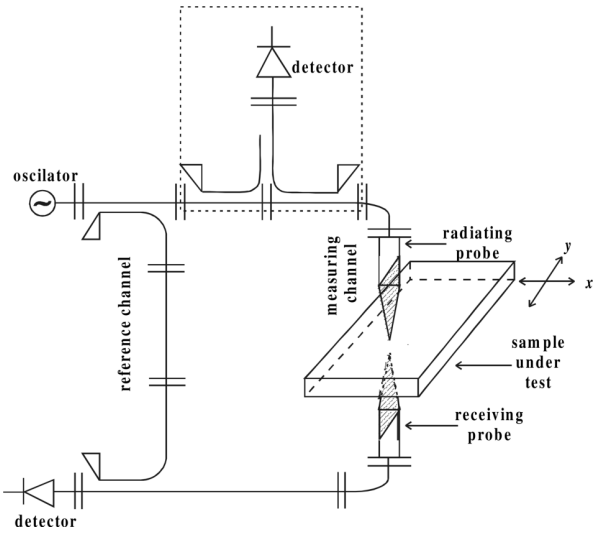

Fig. 12. Schematic diagram of the millimetre wave bridge.

4.2. Nondestructive material homogeneity characterization by scanning millimetre wave beam

The relatively short wavelength of the millimetre wave makes it possible to utilize such waves for non-destructive homogeneity characterization of a very wide spectrum of materials [31]. The main idea of the experiment is the local excitation of millimetre waves in the tested sample and the measurement of transmitted (reflected) amplitude and phase at different locations. A simplified schematic diagram of the experimental set-up is shown in Fig. 12. In essence, this is a millimetre wave bridge consisting of a reference signal channel and a measurement channel. The part of the schematic diagram marked by the dashed line corresponds to a bridge making reflectivity measurements. In such a case, the radiating probe also acts as the receiving antenna for the reflected wave. A testing sample is placed between the special dielectric waveguide probes which provide both the local excitation and reception of the low power millimetre waves ($f = 120$ GHz). The sample can be moved by the scanning mechanism relative to the exciting and receiving probes in the x–y plane. Changes of the electric or dielectric parameters in the sample area cause changes in the amplitude and phase of the transmitted (reflected) signal. By probing the sample at different points with the millimetre wave beam, information can be obtained about the homogeneity of the sample. All measurement processes are computer controlled and the measurement results are compiled in the computer. Some measured material homogeneity results are presented below.

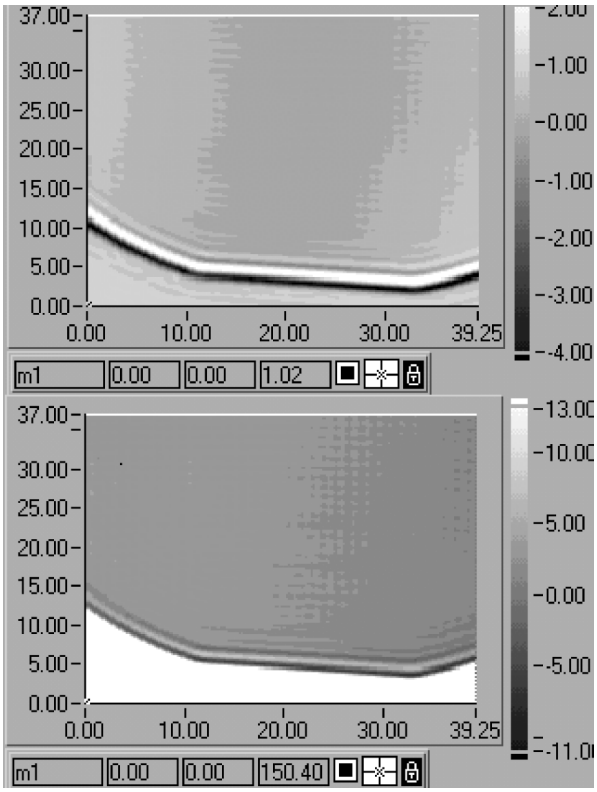

Fig. 13. Transmitted wave amplitude (top) and phase (bottom) images of the sapphire substrate. The measurement units are decibels and degrees, respectively. Thickness of the substrate is 0.43 mm. The scanning area is 37.00×39.25 mm^2.

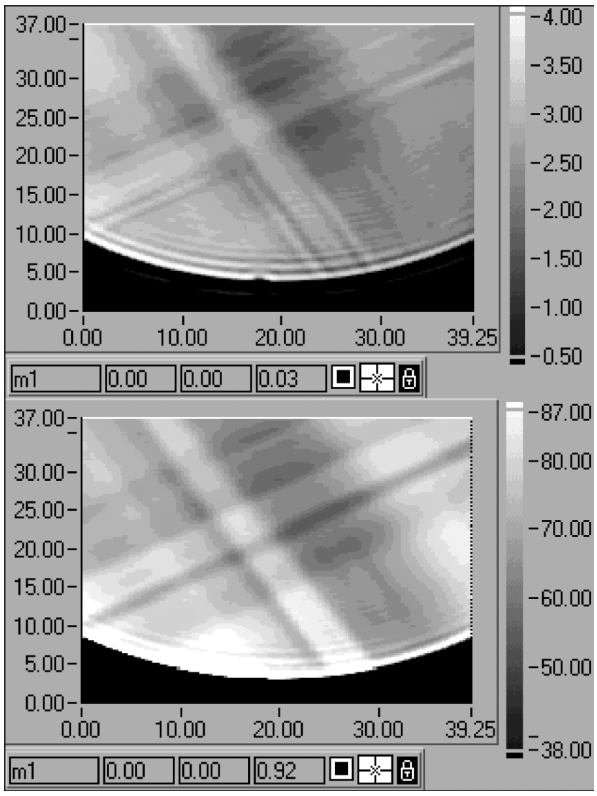

Fig. 14. Transmitted wave amplitude (top) and phase (bottom) images of the $LaAlO_3$ substrate. The measurement units are decibels and degrees, respectively. Thickness of the substrate is 0.50 mm. The scanning area is 37.00×39.25 mm^2.

The measured homogeneity of sapphire and $LaAlO_3$ substrates are shown in Figs. 13 and 14, respectively. The tops and bottoms of the pictures correspond to the transmitted millimetre wave amplitude and phase images of the measured substrates. Both the amplitude and the phase images in Fig. 13 demonstrate the high homogeneity of the sapphire substrate. In contrast, for the case of $LaAlO_3$ substrate (Fig. 14), the crystal twinning associated with lattice structure inhomogeneity is seen very clearly. In addition, it is worth noting that the millimetre waves allow one also to observe the mechanical defects inside dielectrics. Even more, this option has several advantages in comparison to conventional ultrasonic testing. First of all, we bear in mind their relatively high penetration depth due to which they can provide the image of bulk non-homogeneity. The other merit over the ultrasound approach is a good transmission across solid–air boundaries. The possibility of application of these waves for detection of mechanical defects inside the crystal is illustrated by the observed spot in the millimetre wave image of the SiC substrate (Fig. 15). The observed defect is related with the wave scattering by microslits in the crystal volume; according to our estimates, the dimensions of the microslits are less than 1 mm.

The reflection of electromagnetic waves from conducting surfaces is determined by their resistivity. Thus, the measurements of the reflected wave amplitude can produce a resistivity map. This can be seen very clearly in Fig. 16 where a metal mirror surface with different resistivity was scanned by a millimetre wave beam and the corresponding changes in the reflection were detected.

5. Interaction of X-ray radiation with $Al_xGa_{1-x}As$ structures

Semiconductor-based sensors of ionizing radiation are one of the essential components in X-rays equipment or similar set-ups using ionizing illumination. As it is know, such apparatus are widely used in medicine, material diagnostics, environment monitoring, etc. In many cases, the application flexibility is limited namely by detection systems since a variety of the illumination parameters like diameter of flux, intensity, quantum energy, etc. requires to adapt sensors to particular systems

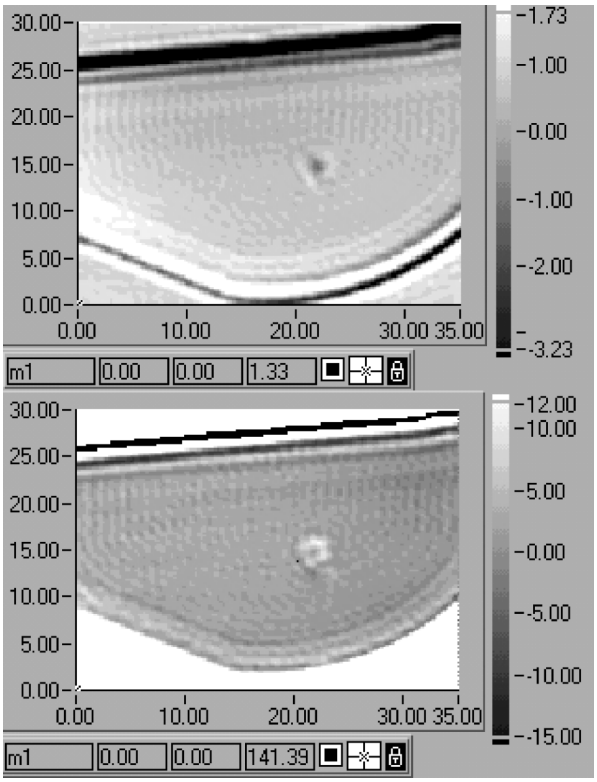

Fig. 15. Transmitted millimetre wave amplitude (top) and phase (bottom) images of a mechanical defect in the SiC substrate. The measurement units are decibels and degrees, respectively. Thickness of the substrate is 0.50 mm. The scanning area is 30.00×35.00 mm^2.

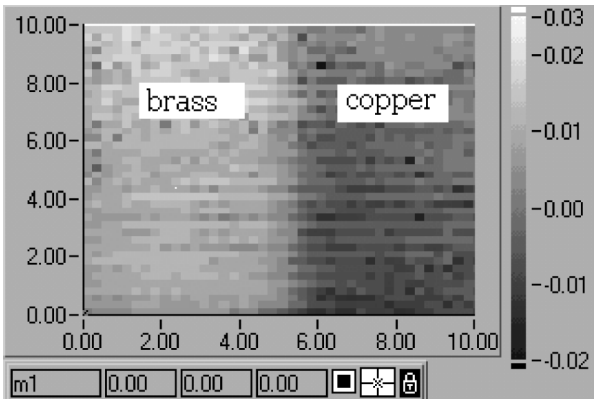

Fig. 16. Reflected wave amplitude image of the mirror made of two different metals (copper and brass). Amplitude changes are in decibels. The scanning area is 10×10 mm^2.

designed for concrete tasks. That is why huge efforts are given to find novel materials suitable for fabrications of arrays to record an X-ray image. One of most promising materials is assumed to be the graded-gap $Al_xGa_{1-x}As$ compounds.

The X-ray detectors based on the graded-gap $Al_xGa_{1-x}As$ layers were proposed and first produced in 1998 [32, 33]. The choice of the material was motivated by an efficient absorption of X-ray radiation and a high radiative recombination rate in $Al_xGa_{1-x}As$ together with specific properties of a graded-gap layer, such as a wide gap optical window and an internal graded-gap field. These advantages allow one to construct different types of ionizing radiation detectors with optical and electrical responses [34–36].

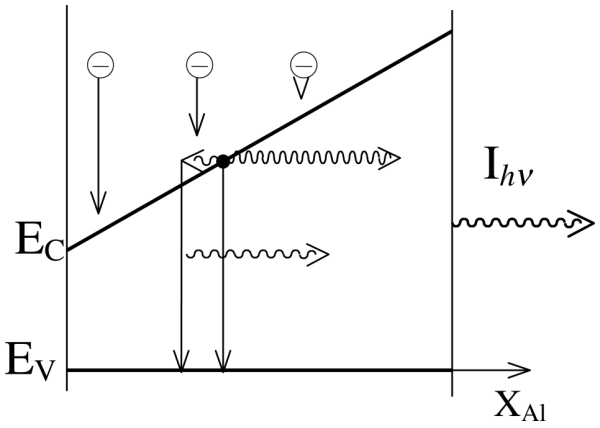

Fig. 17. Schematic view of the band structure of the graded-gap $Al_xGa_{1-x}As$ X-ray detector with optical response.

Conversion of the ionizing radiation generated charge to recombination light is an operating mechanism of the detector with optical response. Detector with optical response does not need an electric supply and electric signal preamplifiers. This circumstance permits one to get a high density of the detector integration (there is no need for pixel array fabrication) that is important for many practical applications. The material of detector is a doped semiconductor of high conductivity, therefore, the problem in preparation of a high resistivity very pure material disappears.

We have fabricated X-ray imaging detectors with optical response on the basis of Zn doped graded-gap $Al_xGa_{1-x}As$ layers of 20–100 μm thickness grown by liquid phase epitaxy and removed from GaAs substrates. Detectors area with homogeneous luminescence was 2×3 cm^2. A schematic band structure of the detector with optical response is shown in Fig. 17.

The $Al_xGa_{1-x}As$ layer of $d = 100$ μm absorbs up to 95% of X-ray power with energy of $E_X < 20$ keV. Therefore, the $Al_xGa_{1-x}As$ layer of $20-100$ μm thickness can be used to detect a soft part of X-ray source spectra with energy less than 30 keV [34]. The optical image of X-ray intensity was detected by a charge-coupled device (CCD) camera, and the data was read by a personal computer (Fig. 18). Several other methods of optical response detection with fibre line or mirror system can be used.

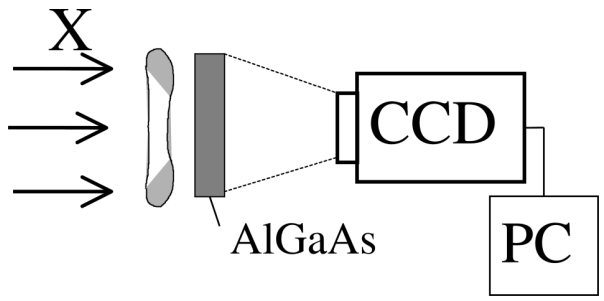

Fig. 18. Set-up for the $Al_xGa_{1-x}As$ X-ray imaging detector.

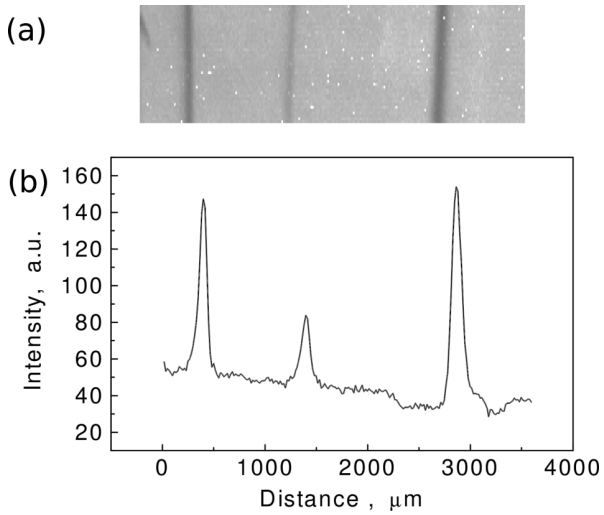

Fig. 19. (a) The X-ray luminescense view of three metal wires of thickness 30, 50, 100 μm and (b) luminescense intensity distribution.

The external efficiency of X-ray–light conversion of the $Al_xGa_{1-x}As$ detector $K_{\rm ef}$ is determined by the part of the X-ray photon energy absorbed in the $Al_xGa_{1-x}As$ layer a_x, the internal quantum efficiency α_c, and the efficiency γ of light output from the graded-gap $Al_xGa_{1-x}As$ structure:

$$K_{\rm ef} = a_{\rm X}\alpha_c\gamma\,. \tag{4}$$

The main factor reducing the conversion efficiency $K_{\rm ef}$ is the low light output efficiency from the crystal caused by the small angle of total internal reflection ($\theta = 16^\circ$).

The X-ray luminescence images of different objects obtained by the CCD camera were used to determine the contrast and spatial image resolution. It is shown that the 1.5% luminescence signal change can be recognized on a PC monitor. The X-ray luminescence image on the PC monitor and luminescence intensity distribution of three metal wires (Fig. 19) demonstrates the high spatial resolution of the detector.

Two processes, the diffusion of generated charge and the broadening of light beam, cause the blurring of X-ray image in the detectors. The value of spatial resolution mainly depends on the thickness of the graded-gap $Al_xGa_{1-x}As$ layer. For instance, the spatial resolution of 10 LP/mm obtained for the detector of 50 μm thickness and 25 LP/mm for the detector of 18 μm thickness provides a 30% contrast [37]. It is satisfying to note that this value of contrast is definitely enough for the analysis of X-ray image.

While aiming to eliminate the internal reflection of light-emitting structures and to increase radically the X-ray detector sensitivity, new non-uniformly doped graded-gap $Al_xGa_{1-x}As$ structures with electric response were proposed and investigated [38].

Two types of graded-gap $Al_xGa_{1-x}As$ structures were studied, n-GaAs–p-$Al_xGa_{1-x}As$ structures containing a p–n junction at the wide energy gap side ($x = 0.4$) of the graded-gap layer and p-$Al_xGa_{1-x}As$–n-GaAs structures with a p–n junction at the narrow energy gap side ($x = 0$) of the graded-gap layer. Figure 20 shows schematically the band diagrams of the grown structures. The operating mechanisms of these two types of structure are different. In the structures with a p–n junction at the wide gap side (Fig. 20(a)), X-rays excite luminescence in the graded-gap $Al_xGa_{1-x}As$ layer. This luminescence is transmitted through a wide-gap optical window to a GaAs p–n junction. The p–n junction photovoltaic $U_{\rm p}$ or current response $I_{\rm ph}$ to the X-ray luminescence is measured then. In p-$Al_xGa_{1-x}As$–n-GaAs structures with p–n junction in the narrow gap side (Fig. 20(b)), electron–hole pairs generated by X-rays in the graded-gap layer are extracted from $Al_xGa_{1-x}As$ layer and collected at the p–n junction by internal graded-gap field before recombination. Note that the generated carriers are collected without application of any external bias voltage.

Figure 21 illustrates the measured dependences of $I_{\rm ph}$ and $U_{\rm p}$ on the X-ray power W at the surface of the $Al_xGa_{1-x}As$/GaAs detectors. The power $W_{\rm X\,abs}$ absorbed in the detector is

$$W_{\rm X\,abs} = W\,S\,a_x\,, \tag{5}$$

where S is the detector surface area and a_x is the fraction of the X-rays absorbed in the $Al_xGa_{1-x}As$ layer. For a thick (50 μm) detector with a p–n junction, $a_x \approx 0.78$ and $S_{pn} = 0.35$ cm^2. A thin (15 μm) detector with a n–p junction has $a_x \approx 0.45$ and $S_{np} = 0.10$ cm^2. The a_x is estimated from the absorption of an X-ray beam with an energy $E_{\rm X} \approx 8$ keV. In this estimate the experimental data (Fig. 21) for the ampere–watt sensitivities are $\beta_j = 0.078$ A/W for the thick (50 μm) detector and $\beta_j = 0.226$ A/W for the thin (15 μm) one.

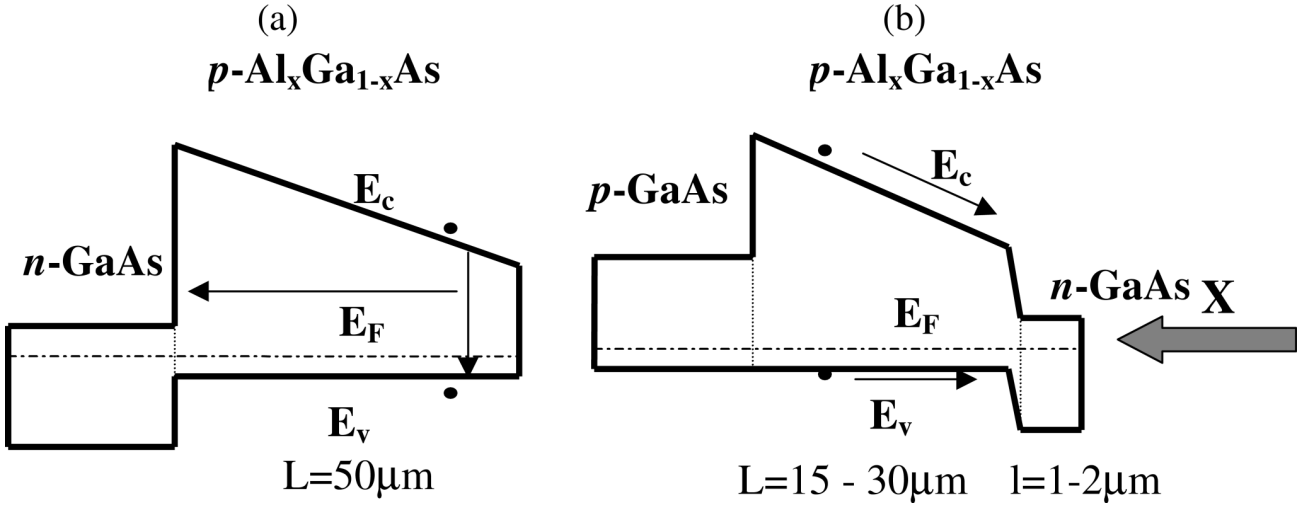

Fig. 20. Schematic band diagrams of (a) n-GaAs-p-$Al_xGa_{1-x}As$ structure with a p–n junction at the wide energy gap side ($x = 0.4$) of the graded-gap layer, (b) p-$Al_xGa_{1-x}As$-n-GaAs structure with a p–n junction at the narrow energy gap side ($x = 0$) of the graded-gap layer.

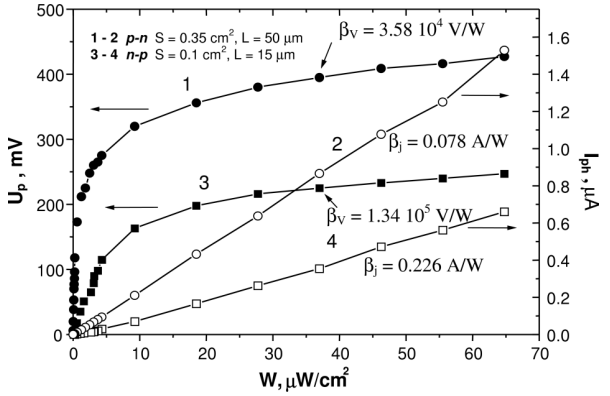

Fig. 21. The current $I_{\rm ph}$ and voltage $U_{\rm p}$ response dependence on the X-ray power at the surface of the thick ($L = 50$ μm) $Al_xGa_{1-x}As$ / GaAs detector with a p–n junction at the wide energy gap side (curves *1*, *2*) and the thin ($L = 15$ μm) detector with a p–n junction at the narrow energy gap side (curves *3*, *4*).

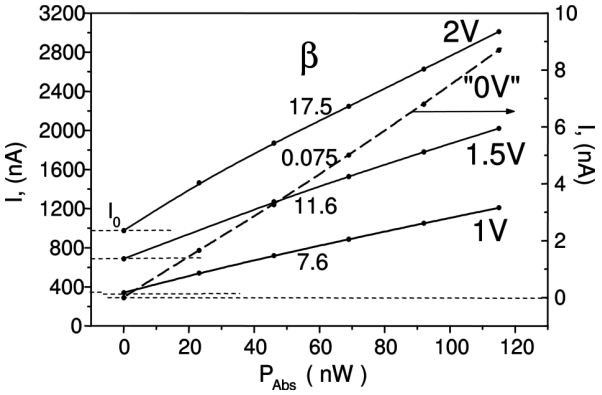

Fig. 22. The short current I_D through the n^--GaAs / p^+-$Al_xGa_{1-x}As$ heterostructure as a function of absorbed X-ray power at different bias voltages (V) and currents (I_0). The curves are labelled by the current against absorbed power sensitivity. The dashed line corresponds to I_D ($P_{\rm abs}$) without application of any bias (right scale). The dotted lines indicate the levels of bias current I_0 at $P_{\rm abs} = 0$.

The value of β_j in the thin (15 μm) layer is near to the value of 0.25 A/W, corresponding to a hundred percent collection of charge generated in the detector bulk. It is worth noting that 100% charge collection efficiency is achieved now in a 27 μm thick $Al_xGa_{1-x}As$ detector [39].

The observed volt–watt sensitivity β_v is the largest at low absorbed power. At $W_{\rm X\,abs} \approx 10^{-7}$ W the measured β_v is $\approx 5 \cdot 10^5$ V/W, and at $W_{\rm X\,abs} \approx 2 \cdot 10^{-6}$ W it is $\beta_v \approx 1.1 \cdot 10^5$ V/W.

The new charge multiplication method by increasing the n^-/p^+ heterojunction reverse current is implemented in the n-GaAs / p^+-$Al_xGa_{1-x}As$ structure consisting of thin ($l_n < 10^{-4}$ cm) low-doped ($n = 10^{15}$ cm^{-3}) n-GaAs layer grown at the narrow-gap side of high-doped ($p = 10^{18}$ cm^{-3}) p^+-$Al_xGa_{1-x}As$ layer [40].

Figure 22 shows the dependence of the experimentally measured current through the device on the absorbed X-ray power at different bias current I_0. The X-ray tube with a Cu anode has been used as an X-ray radiation source. The measured current sensitivity β at the zero bias current ($I_0 = 0$) is equal to $I_{\rm X}/P_{\rm abs} = 0.075$ A/W. This corresponds to the charge collection efficiency $\eta = 0.33$. The multiplication of the collected charge increases with increasing I_0 and achieves the value $K = 234$ at $I_0 = 0.97$ μA. Correspondingly, the current over absorbed power sensitivity increases by a factor of 234 and achieves $\beta = 17.5$ A/W. This is 70 times larger than the sensitivity $\beta = 0.25$ A/W in the case of 100% collection of charge generated in the $Al_xGa_{1-x}As$.

The graded-gap $Al_xGa_{1-x}As$ structure can be used

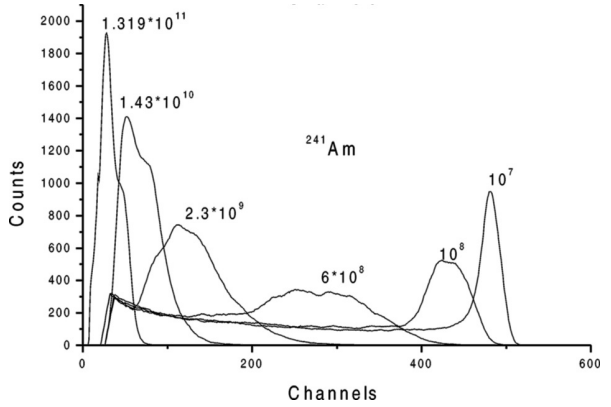

Fig. 23. The amplitude spectra of graded-gap detector current response to ^{241}Am alpha particle irradiation at different doses. Doses of preliminary alpha particle irradiation (particles/cm^2) are shown at the curves.

also as a high efficiency single particle detector (^{241}Am alpha particles) operating without application of any bias. The results of alpha particle irradiation on the measured energy spectra of ^{241}Am alpha particles using the graded-gap $Al_xGa_{1-x}As$ structure are shown in Fig. 23. Because of the high efficiency of generated charge collection, high resolution of alpha particle energy spectra is obtained before irradiation [41]. The irradiation by alpha particles causes the increase in both the non-radiative and radiative recombination rate in a graded-gap $Al_xGa_{1-x}As$ layer and reduces the efficiency of charge collection. As a result, the detector response decreases.

It was obtained [42] that the current response of the graded-gap $Al_xGa_{1-x}As$ detector decreases by a factor of 7 at the alpha particle irradiation dose of 10^{10} cm^{-2}. The optical response, however, decreases by only 1.5 times at the same irradiation dose. Finally, it is worth noting that the increase of the radiative recombination rate with irradiation dose is responsible for the far better radiation hardness of the detectors with optical response.

Acknowledgements

We are sincerely thankful to Gintaras Valušis for his good will in preparing the manuscript of the article and contribution on electron gas cooling effect results. Also, we are indebted to the Lithuanian State Science and Studies Foundation for partial support under the contracts ATPP-B-08 and NEPEK-B-13.

References

[1] A. Vebra and J. Pozhela, Investigation of carrier mobility in germanium in high electric fields, Trudy Akademii Nauk Litovskoy SSR B **2**(25), 99–105 (1961) [in Russian].

[2] V. Dienys and J. Požela, *Hot Electrons* (Mintis, Vilnius, 1971) [in Russian].

[3] T. Banys, J. Paršeliūnas, and J. Pozhela, Absolute negative resistance of gallium arsenide under the influence of strong microwave field, Fiz. Tekh. Poluprovodn. (Sov. Phys. Semicond.) **5**, 1990–1992 (1971).

[4] T. Banys, J. Paršeliūnas, and J. Pozhela, High-voltage microwave emf in GaAs, Lietuvos Fizikos Rinkinys **11**, 1013–1019 (1971).

[5] J. Pozhela, K. Repšas, and V. Shilalnikas, Hot current carriers in Ge and Si, in: *Proceedings of International Conference on the Physics of Semiconductors*, Exeter, England, 1962, pp. 149–151.

[6] S. Ašmontas, *Electrogradient Phenomena in Semiconductors* (Mokslas, Vilnius, 1984) [in Russian].

[7] J.K. Pozhela, Plasma and Current Instabilities in Semiconductors (Pergamon Press,New York, 1981).

[8] A. Laurinavičius and J. Požela, Investigation of helicon waves from magnetoreflection in InSb samples at microwave frequencies, Lietuvos Fizikos Rinkinys **11**, 65–71 (1971).

[9] J. Požela and R. Tolutis, Investigation of semiconductors by helicon waves, in: *Many-valley Semiconductors* (Mokslas, Vilnius, 1978), pp. 87–142.

[10] L. Laurinavičius and R. Tolutis, Semiconductor alloy resonator-type HF isolators, Electron. Lett. **18**, 243–244 (1982).

[11] L. Laurinavičius and R. Tolutis, Semiconductor valve, Prib. Tekh. Eksp. (Instrum. Exp. Tech. (USSR)) **25**(4), 255 (1982) [in Russian].

[12] A. Šilėnas, J. Požela, V.M. Smith, K. Požela, V. Jasutis, L. Dapkus, and V. Jucienė, Non-uniformly doped gruded-gap $Al_xGa_{1-x}As$ X-ray detectors with high photovoltaic response, Nucl. Instrum. Methods A **487**, 54–59 (2002).

[13] K. Požela, J. Požela, V. Jasutis, L. Dapkus, and A. Šilėnas, New type X-ray detector with optical response, in: *Proceedings of the 24th Workshop on Compound Semiconductors Devices and Integrated Circuits*, Aegean Sea, Greece, May 29 – June 02, 2000, pp. XIV-17–XIV-18.

[14] S. Ašmontas and L. Subačius, Hot electron diffusion coefficient in germanium, Lietuvos Fizikos Rinkinys **17**, 71–78 (1977) [in Russian; English translation in: Sov. Phys. Collection **17**, 43–48 (Allerton Press Inc., New York, 1977)].

[15] S. Ašmontas, J. Požela, L. Subačius, and G. Valušis, Electron gas heating and cooling effects by microwave electric fields in compensated InSb, Solid-State Electron. **31**, 701–703 (1988).

[16] S. Ašmontas, S. Dedulevičius, Ž. Kancleris, L. Subačius, and G. Valušis, Investigation of hot electron relaxation in electric fields in compensated InSb<Cr>, Lietuvos Fizikos Rinkinys **32**, 425–433 (1992) [in Russian; English translation in: Lithuanian J. Phys. **32**, 224–228 (Allerton Press Inc., New York, 1992)].

[17] Z.S. Gribnikov and V.A. Kochelap, Cooling of current carriers scattering their energy on the optical lattice vibrations, Sov. Phys. JETP **12**(3), 1046–1056 (1970).

[18] S. Ašmontas and L. Subačius, Hot electron thermoemf in compensated InSb<Cr>, Fiz. Tekh. Poluprovodn. (Sov. Phys. Semicond.) **16**, 40–47 (1982).

[19] S.P. Ashmontas, Yu.K. Pozhela, and L.E. Subachyus, Heating and cooling of electron gas in electric fields in compensated indium antimonide, JETP Lett. **33**(11), 564–567 (1981).

[20] V. Bareikis, R. Katilius, and R. Miliušytė, *Fluctuation Phenomena in Semiconductors in Nonequilibrium State* (Mokslas, Vilnius, 1989).

[21] S. Ašmontas, J. Liberis, L. Subačius, and G. Valušis, Electron gas cooling studied by measurements of noise temperature, Semicond. Sci. Technol. 7, B331–B333 (1992).

[22] S. Ašmontas, K. Požela, and K. Repšas, Investigation of I–V characteristics of Ge and Si asymmetrically necked samples, Lietuvos Fizikos Rinkinys **15**, 249–258 (1975).

[23] S. Ašmontas, Study of electron heating by nonuniform electric fields in n-Si, Phys. Status Solidi A **31**, 409 (1975).

[24] S. Ašmontas, J. Pozhela, and K. Repšas, *Phenomenon of Electromotive Force and Asymmetry of Electrical Conductivity in Uniform Isotropic Semiconductor*, Diploma of discovery No. 185, Bulletin of Inventions (39), 1 (1977) [in Russian].

[25] S. Ašmontas, A. Juozapavičius, D. Seliuta, E. Širmulis, V. Tamošiūnas, G. Valušis, and K. Köhler, In-plane shaped GaAs/AlGaAs modulation-doped structures: Physics and applications for THz / subTHz sensing, in: *Trends in Semiconductor Research*, ed. T.B. Elliot (Nova Science Pub. Inc., New York, 2005) pp. 59–80.

[26] E.D. Palik and J.K. Furdyna, Infrared and microwave magnetoplasma effects in semiconductors, Rep. Prog. Phys. **33**(12), 1193–1322 (1970).

[27] A. Laurinavičius and J. Požela, Contactless measurement of free charge carrier distribution in volume of the narrow gap semiconductors, Prib. Tekh. Eksp. (Instrum. Exp. Tech. (USSR)) **19**(4), 241–242, (1976) [in Russian].

[28] A. Laurinavičius, J. Požela, and R. Tolutis, Helicon diagnostics of narrow gap semiconductor quality, in: *Proceedings of the 10th World Conference on Non Destructive Testing* **3** (Moscow, 1982), pp. 265–273.

[29] A. Laurinavičius and J. Požela, Helicon diagnostics, Nauka v SSSR, No. 6, 34–38 (1987) [in Russian].

[30] A. Laurinavičius, P. Malakauskas, and J. Požela, Semiconductor non-destructive testing by helicon waves, Int. J. Infrared Millimeter Waves **8**(5), 573–582 (1987).

[31] A. Laurinavičius, T. Anbinderis, O. Martjanova, J. Prišutov, A. Abrutis, and A. Teišerskis, Non-destructive material homogeneity characterization by millimeter waves, Int. J. Infrared Millimeter Waves **22**(7), 961–965 (2001).

[32] K. Požela, J. Požela, and V. Jucienė, Light emitted GaAs detectors, Nucl. Instrum. Methods A **410**, 111–114 (1998).

[33] J. Požela, K. Požela, A. Šilėnas, V. Juciene, L. Dapkus, V. Jasutis, G. Tamulaitis, A. Žukauskas, and R.-A. Bendorius, The AlGaAs light emitting particle detector, Nucl. Instrum. Methods A **434**, 169–172 (1999).

[34] K. Požela, J. Požela, A. Šilėnas, V. Jasutis, L. Dapkus, and V. Jucienė, The $Al_xGa_{1-x}As$ X-ray imaging detector, Nucl. Instrum. Methods A **460**, 119–122 (2001).

[35] A. Šilėnas, J. Požela, K. Požela, V. Jasutis, L. Dapkus, and V. Jucienė, Graded-gap $Al_xGa_{1-x}As$ X-ray detectors with fast photovoltaic response, Mater. Sci. Forum **384–385**, 287–290 (2002).

[36] J. Požela, K. Požela, A. Šilėnas, V. Jasutis, L. Dapkus, A. Kinduris, and V. Jucienė, A graded-gap detector of ionizing radiation, Semicond. **36**, 116–120 (2002).

[37] A. Šilėnas, J. Požela, K. Požela, L. Dapkus, and V. Jucienė, High spatial resolution graded-hap AlGaAs X-ray detector, in: *Abstracts of 7th International Workshop on Radiation Imaging Detectors*, 4–7 July 2005, Grenoble, France, p. 27.

[38] A. Šilėnas, J. Požela, K. Požela, V. Jasutis, L. Dapkus, and V. Jucienė, Non-uniformly-doped graded-gap AlGaAs X-ray detectors with high photovoltaic response. Nucl. Instrum. Methods A **487**, 54–59 (2002).

[39] A. Šilėnas, Graded-gap $Al_xGa_{1-x}As$ ionizing radiation detectors, Lithuanian J. Phys. **44**, 49–57 (2004).

[40] A. Šilėnas, K. Požela, L. Dapkus, V. Jasutis, V. Jucienė, J. Požela, and K.M. Smith, Graded-gap $Al_xGa_{1-x}As$ X-ray detector with collected charge multiplication, Nucl. Instrum. Methods A **509**, 30–33 (2003).

[41] L. Dapkus, K. Požela, J. Požela, A. Šilėnas, V. Jucienė, and V. Jasutis, Behavior of graded-gap detectors of ionizing radiation under irradiation with alpha particles, Semicond. **38**(9), 1111–1114 (2004).

[42] A. Šilėnas, L. Dapkus, K. Požela, J. Požela, V. Jucienė, and V. Jasutis, Radiation hardness of graded-gap $Al_xGa_{1-x}As$ X-ray detectors, Nucl. Instrum. Methods A **546**, 228–231 (2005).

MIKROBANGŲ IR RENTGENO SPINDULIUOTĖS SUKELIAMI REIŠKINIAI PUSLAIDININKIUOSE

S. Ašmontas [a,b], A. Laurinavičius [a], J. Paukštė [b], A. Šilėnas [a]

[a] *Puslaidininkių fizikos institutas, Vilnius, Lietuva*
[b] *Kauno technologijos universiteto Panevėžio institutas, Panevėžys, Lietuva*

Santrauka

Pateikti mikrobangų ir Rentgeno spinduliuotės sąveikos su įvairiais puslaidininkiais eksperimentiniai tyrimai, atlikti Puslaidininkių fizikos institute, pradedant novatoriškais J. Poželos darbais ir baigiant paskutiniųjų metų rezultatais. Pagrindinis dėmesys buvo skirtas mikrobangų metodui, leidžiančiam nustatyti karštųjų elektronų difuzijos koeficientą puslaidininkiuose, ir bigradientiniam efektui, kuris 1977 metais buvo pripažintas atradimu. Taikomasis šių tyrimų pobūdis atskleidžiamas, apžvelgiant neardančius paviršiaus puslaidininkių parametrų nustatymo metodus, panaudojant helikonines bangas arba lokaliai sužadinant milimetrines bangas bandiniuose, bei Rentgeno spinduliuotės konversiją į infraraudonąją šviesą varizoniniuose $Al_xGa_{1-x}As$ dariniuose, įgalinančią nuskaityti Rentgeno vaizdą įprastine CCD kamera.